Geomaterials, 2023, 13, 91-108
https://www.scirp.org/journal/gm
ISSN Online: 2161-7546
ISSN Print: 2161-7538

Determination of Curie Point Depth and Heat Flow Using Airborne Magnetic Data over the Kom-Ombo and Nuqra Basins, Southern Eastern Desert, Egypt

Ahmed Tarshan, Asmaa A. Azzazy, Ali M. Mostafa, Ahmed A. Elhusseiny

Airborne Geophysics Department, Nuclear Materials Authority, Cairo, Egypt
Email: ahmednoureldin1985@gmail.com

How to cite this paper: Tarshan, A., Azzazy, A.A., Mostafa, A.M. and Elhusseiny, A.A. (2023) Determination of Curie Point Depth and Heat Flow Using Airborne Magnetic Data over the Kom-Ombo and Nuqra Basins, Southern Eastern Desert, Egypt. *Geomaterials*, **13**, 91-108.
https://doi.org/10.4236/gm.2023.134007

Received: August 5, 2023
Accepted: September 25, 2023
Published: September 28, 2023

Copyright © 2023 by author(s) and Scientific Research Publishing Inc.
This work is licensed under the Creative Commons Attribution International License (CC BY 4.0).
http://creativecommons.org/licenses/by/4.0/
Open Access

Abstract

The Kom-Ombo and Nuqra basins in southern Egypt have recently been discovered as potential hydrocarbon basins. The lack of information about the geothermal gradient and heat flow in the study area gives importance to studying the heat flow and the geothermal gradient. Several studies were carried out to investigate the geothermal analyses of the northwestern desert, as well as the west and east of the Nile River, using density, compressive wave velocity, and bottom hole temperature (BHT) measured from deep oil wells. This research relies on spectral analysis of airborne magnetic survey data in the Kom-Ombo and Nuqra basins in order to estimate the geothermal gradient based on calculating the depth to the bottom of the magnetic source that caused the occurrence of these magnetic deviations. This depth is equal to the CPD, at which the material loses its magnetic polarisation. This method is fast and gives satisfactory results. Usually, it can be applied as a reconnaissance technique for geothermal exploration targets due to the abundance of magnetic data. The depth of the top (Z_t) and centroid (Z_0) of the magnetic source bodies was calculated for the 32 windows representing the study area using spectral analysis of airborne magnetic data. The curie-isotherm depth, geothermal gradient, and heat flow maps were constructed for the study area. The results showed that the CPD in the study area ranges from 13 km to 20 km. The heat flow map values range from 69 to 109 mW/m^2, with an average of about 80 mW/m^2. The calculated heat flow values in the assigned areas (A, B, C, and D) of the study area are considered to have high heat flow values, reaching 109 mW/m^2. On the other hand, the heat flow values in the other parts range from 70 to 85 mW/m^2. Since heat flow plays an essential role in the maturation of organic matter, it is recommended that hydrocarbon accumulations be located in places with high heat flow values, while deep drilling of hydrocarbon wells is recommended in places with low to moderate heat flow values.

Keywords

Curie Point, Heat Flow, Airborne Magnetic Data, Nuqra Basin, Kom-Ombo Basin, Eastern Desert

1. Introduction

Several stresses during the Late Cretaceous affected the sedimentary cover succession in Egypt and were attributed to the collision between the African and Eurasian plates, leading to shortening in North Africa and the formation of large-scale E-W to ENE strike-slip faults in Afro-Arabia ([1] [2] [3]).

This collision occurred concurrently with crustal extensions along north-west trending faults that continued to the Oligo-Miocene, resulting in the formation of the Red Sea Basin, which stretches from the northwest to Kom-Ombo in the southeast for more than 250 km and is dissected by numerous northeastern and southwestern trending faults similar in size to the Gulf of Suez fault ([3]-[8]).

The Kom-Ombo and Nuqra basins are considered parts of the continental rift that was formed as a result of the Red Sea rift [8]. The study of the Kom-Ombo and Nuqra basins indicates their hydrocarbon potential [3]. The Kom-Ombo and Nuqra basins are located in southern Egypt (**Figure 1**), where the Nile River separates the Kom-Ombo basin to the west from the Nuqra basin to the east.

The potential of hydrocarbons has been widely studied and evaluated recently in numerous studies (e.g., [3] [9]-[17]). Due to the importance of the Kom-Ombo and Nuqra basins, it is worthwhile to study the geothermal gradient and heat flow for further exploration.

Hosney (2000) [18] used density and compressional wave velocity to investigate heat flow east and west of the Nile River. It was concluded that the northern part of the western part of the Nile River is characterized by a low heat flow (46 mW/m^2), while the eastern part of Egypt is characterized by a high heat flow reaching (80 - 130 mW/m^2).

Mohamed *et al.* (2015) [19] studied the geothermal gradient in the northern part of the Western Desert. The study relied on bottom-hole temperatures recorded from 149 deep oil wells. The study showed that there is a decrease in the geothermal gradient by about 30˚C/km in the northern part of the Western Desert.

Saada (2016) [20] studied the heat flow and geothermal gradient over the northern part of the Western Desert (between latitudes of 30˚ and 32˚ and longitudes of 26˚ and 30˚). This study is a regional one based on the spectral analysis of airborne magnetic data. He concluded that the depth of magnetic objects increases from 24.5 km in the southern part to 33 km in the northern part. The calculated surface heat flow value ranges from about 56 to 42 mW/m^2.

No research study was conducted in the study area to study the heat flow and geothermal gradient. Calculating heat flow is critical and necessary for oil and gas prediction [21], as the Kom-Ombo and Nuqra basins are important and potential hydrocarbon areas. Due to the lack of wells drilled in this area and the absence of information about the heat flow over the Kom-Ombo and Nuqra basins, this research was conducted to evaluate the geothermal gradient and the surface heat flow over the Kom-Ombo and Nuqra basins. The idea of this research is to use airborne magnetic data to determine the depth to the top and bottom (basal) of the magnetic source objects to estimate the geothermal gradient. This depth is equal to the Curie point depth (CPD), at which the material loses its magnetic polarization.

2. Study Area and Geological Features

The study area is located in southern Egypt, between latitudes 23˚43'31.00" and 25˚10'59.94" and longitudes 32˚28'45.90" to 34˚06'19.97" (**Figure 1**). The two basins of Kom-Ombo and Nuqra Basins are divided by the Nile River, the Kom-Ombo basin to the west and the Nuqra Basin to the east (**Figure 1**). The surface geological map (**Figure 2**) shows that the outcrops of the study area vary in age from Quaternary to Precambrian. The Quaternary and Protonile deposits cover the central part of the study area. The Nile silt and Neonile deposits are scattered along the Nile River bank, where the Neonile deposits extend further to the east until they turn into Protonile deposits, which begin to spread in the central part of the study area.

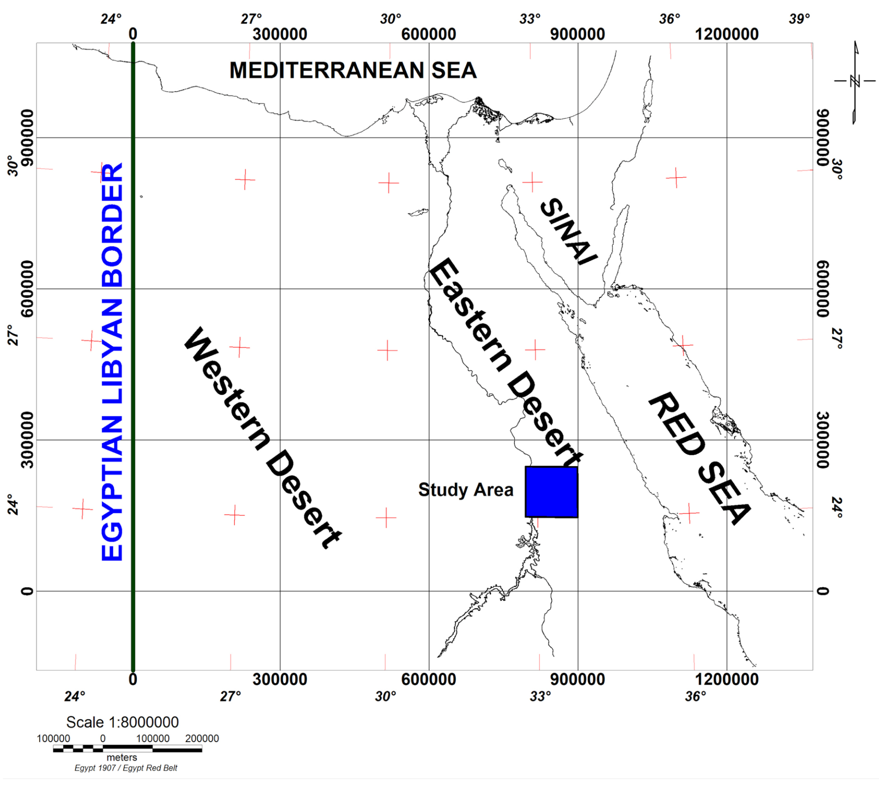

Figure 1. A map of Egypt showing the location of the study area.

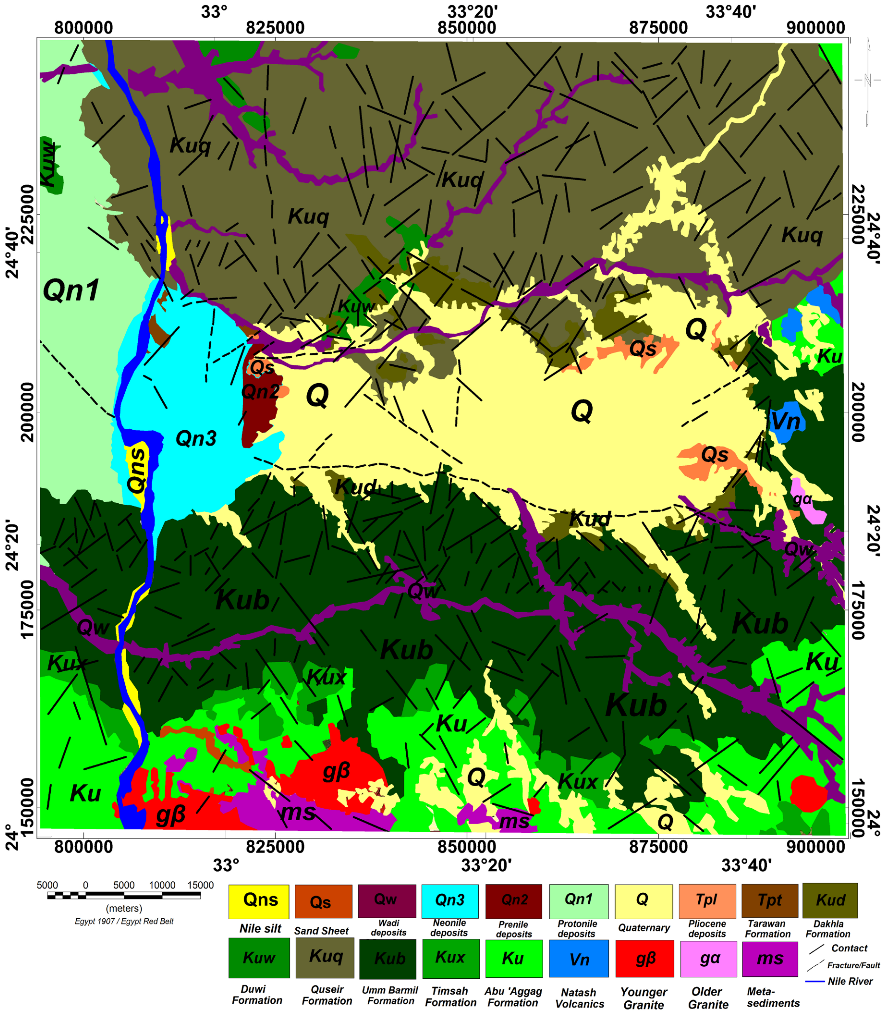

Figure 2. Geologic map of the study area (modified after Conoco, 1987).

The Pliocene deposits are found in the eastern part of the study area. The Paleocene deposits are represented by the Tarawan Formation. This formation is laterally replacing the upper part of the Dakhla Formation [22].

The Upper Cretaceous age covers the northern and southern parts of the area and is represented by the Dakhla Formation, the Duwi Formation, the Quseir Formation, the Umm Barmil Formation, the Timsah Formation, and the Abu Aggag Formation. The Dakhla Formation is composed of dark-grey oscillating marine shale with calcareous intercalations. The Duwi formation is composed of phosphate beds, glauconitic sandstone, and grey shale. On the other hand, the Quseir formation consists of varicolored shale, siltstone, and flaggy sandstone, containing freshwater gastropods, plant remains, and vertebrate remains. The Umm Barmil Formation consists of fluviatile sandstone that becomes more marine towards the north [22].

The Timsah Formation consists mainly of a deltaic sequence of shale, siltstone, and sandstone with two major oolitic iron-ore beds. The Abu Aggag Formation consists of fluvial deposits with cross-bedded sandstone, ripple-laminated sandstone, and lenticular sand bodies. The southwestern part is characterized by the existence of the exposed basement to the surface, such as Natash Volcanics, which is basic to acidic, alkaline undeformed volcanic rocks, metasediments, and calc-alkaline, weakly deformed granitic rocks [22].

The subsurface stratigraphic sequence is described by the presence of a good thickness of the upper Cretaceous sequence. The Upper Cretaceous sequence consists of the Kom-Ombo Formation. This formation is divided into three clastic members known as Kom-Ombo members A, B, and C, which were deposited locally in the Early Berriasian age in the Nile's west. The Kom-Ombo Formation is overlain by the deposition of the Six hills Formation of the Late Berriasian-Barremian, which can be divided into seven members from A (base) to G (top) [3].

In the (Albian-Cenomanian), the Abu Ballas Formation is unconformably overlies the Six Hills Formation, then unconformably overlain by the Sabaya Formation, and it is separated from the overlying Sabaya Formation by a major thrust fault ([23] [24]). The Maghrabi Formation of the Late Cenomanian conformably overlies the Sabaya Formation and underlies other more recent deposits, starting with the Taref Sandstone Formation to the Duwi Formation, which consists of phosphate beds, glauconitic sandstone, and grey shale. The Duwi Formation is overlain by the Dakhla Formation and the Esna Formation, which are mainly composed of dark-grey marine shale [22].

3. Airborne Magnetic Data

An Aero-Service aircraft of the American Western Geophysical Company, 1984 [25], was used for data acquisition to collect the airborne magnetic data of the study area. The survey was conducted under specific conditions, including a flight altitude of about 120 meters of ground clearance. The flight line interval was 1.5 km for the traverse lines and 10 km for the tie lines. The magnetic data was corrected to isolate the component of the magnetic field due to crustal material. Diurnal correction, heading correction, lag correction, and the International Geomagnetic Reference Field (IGRF) were applied to the measured data to produce the corrected magnetic anomalies.

The magnetic fields caused by geologic bodies are deformed by the inclination and declination of the earth's magnetic field. Most magnetic anomalies have both positive and negative counterparts. Therefore, reducing the magnetic data to a magnetic pole (inclination = 90˚) is necessary. In this case, the maximum of the anomalies will be directly over the centre of the causative body. The method of reduction to the pole (RTP) is used to remove this effect, so that the data appear as if observed at the pole.

Blakely (1995) [26] mentioned that the field reduced-to-the pole at a fixed point above the measurement plane in frequency domain is given by,

$$L(\theta)=1\Big/\left[\sin(I_a)-i\cos(I)\cos(D+\theta)\right]^2, \text{ if } (I_a<I),\ \ I_a=I \tag{1}$$

where: I = geomagnetic inclination, I_a = inclination for amplitude correction (never less *I*), D = geomagnetic declination, θ = wavenumber direction and i = imaginary component.

Reduction to the pole has an amplitude component (the sin term) and a phase component [the $i\cos(I)\cos(D+\theta)$ component]. An amplitude inclination of 90˚ causes only the phase component to be applied to the data (no amplitude correction), and a value of 0˚ (zero) causes phase and amplitude components to be applied over the entire range. At low latitudes, it's very sensitive to apply the reduction to the pole due to the distortion of the magnetic anomaly [27]. However, it was found from numerical experiments that there were no significant differences between CDP obtained with and without electrode reduction ([20] [28] [29]).

The RTP map (**Figure 3**) was generated by applying an assumed RTP correction of 4.34˚ declination and 35.92˚ inclination using the Oasis Montaj Program, 2007 [30]. The variations in magnetic intensity of the RTP map (**Figure 3**) suggest a wide variety of different magnetic properties. Positive anomalies are observed at the northwestern, southeastern, southwestern, and northwestern parts of the study area, with values ranging from 100 to 300 nT (**Figure 3**). Magnetic anomalies are produced by the combination of effects from shallow and deep crustal magnetic sources ([20] [31]). Estimating the CPD is related to the deep anomalies; however, the RTP map (**Figure 3**) contains both long wavelength and short-wavelength anomalies. Shallow magnetic bodies generate local magnetic anomalies with a relatively high frequency.

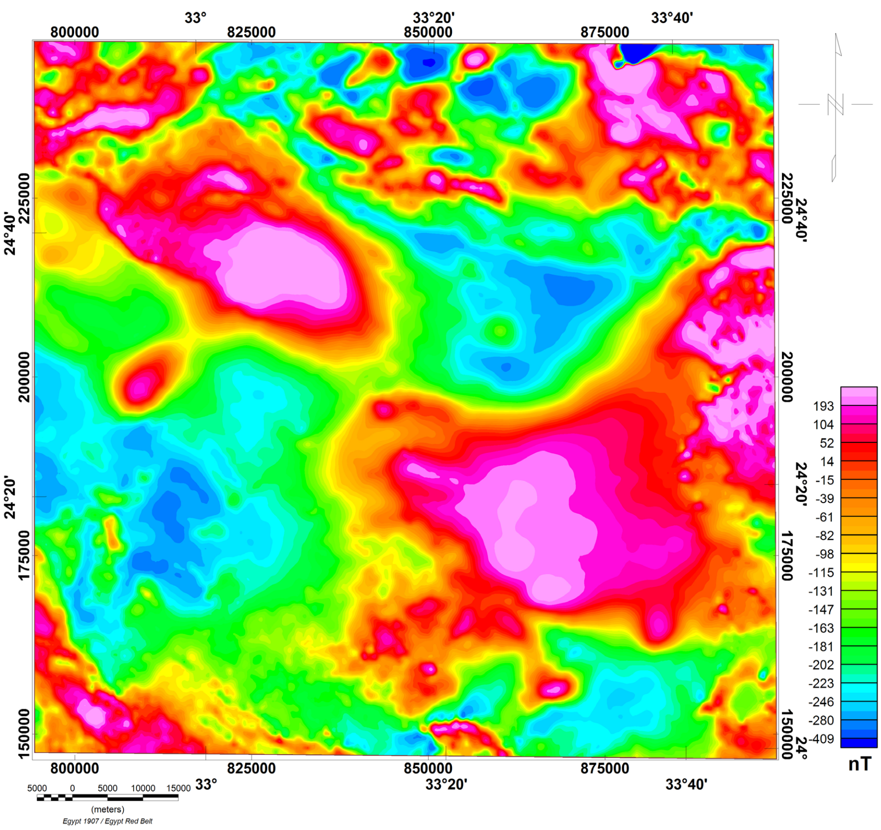

Figure 3. Reduced-to-pole (RTP) map of the study area.

4. Methodology

Spectral analysis of magnetic anomalies is one of the best methods for determining the depth extent of magnetic sources, and it is based on examining the statistical properties of the patterns of magnetic anomalies. This method gives a relationship between the spectrum of magnetic anomalies and the depth of a magnetic source by transforming the spatial data into the frequency domain [32].

Shuey *et al.* (1977) [33] showed that this method is more suitable for regional compilations of magnetic anomalies. The Spectral analysis of magnetic anomaly data was developed in three stages. The first stage was introduced by Spector and Grant (1970) [32]. They described the basic 2-D spectral analysis method and estimated the depth to the top of magnetized rectangular prisms (Z_t) from the slope of the log power spectrum. Secondly, this method was developed by Bhattacharyya and Leu ([34] and [35]). They calculated the depth of the centroid of the magnetic source bodies (Z_0). The third stage was developed by Okubo *et al.* (1985) [28]. They developed a method to estimate the bottom depth of the magnetic bodies (Z_b) using the spectral analysis method of Spector and Grant (1970) [32].

Tanaka *et al.* (1999) [36]; Maden (2010) [37]; and Saibi *et al.* (2015) [38] suppose that the magnetic body infinitely extends in the horizontal direction and that the depth of the magnetic body is very small relative to its horizontal extension scale. According to Bhattacharyya and Leu (1975) [34], the magnetization intensity $M(x,y)$ is a random function of the horizontal directions x and y and can be expressed as follows:

$$\varnothing_{\Delta T}\left(k_x,k_y\right)=\varnothing_M\left(k_x,k_y\right)' F\left(k_x,k_y\right) \tag{2}$$

where $\varnothing_{\Delta T}\left(k_x,k_y\right)$ is the power spectrum of the total magnetic field, $\varnothing_M$ is the power density spectrum of magnetization intensity, and k_x, k_y are wavenumbers in the x and y directions, respectively. Equation (2) can also be written as follows:

$$\varnothing_{\Delta T}\left(k_x,k_y\right)=4\pi^2C_m^2\left|\theta_m\right|^2\left|\theta_f\right|^2\mathrm{e}^{-2|k|Z_t}\left(1-\mathrm{e}^{-|k|(z_b-z_t)}\right)^2 \tag{3}$$

where, θ_f is the power density spectrum of the magnetization; C_m is a proportionality constant; θ_f and θ_m are factors for geomagnetic field direction and magnetization direction, respectively.

z_b and z_t are basal and top depths of the magnetic source, respectively. All terms show radial symmetry and the radial average of θ_f and θ_m is constant. If $M(x,y)$ is a random function, $\varnothing_M\left(k_x,k_y\right)$ is constant, therefore the radial average of $\varnothing_{\Delta T}$ is:

$$\varnothing_{\Delta T}\left(|K|\right)=A\mathrm{e}^{-2|k|Z_t}\left(1-\mathrm{e}^{-|k|(z_b-z_t)}\right)^2 \tag{4}$$

After the appropriate simplification and when the wavelength is smaller than twice the thickness of the magnetic layer, we can obtain an approximate expression of Equation (4), which can be written as:

$$\ln\left[\varnothing_{\Delta T}\left(|K|\right)^{1/2}\right] = \ln B - |K| Z_t \tag{5}$$

where B is a constant. The upper bound of a magnetic source Z_t could be estimated by fitting a straight line through the high-wavenumber part of a radially averaged power spectrum $\ln\left[\varnothing_{\Delta T}\left(|K|\right)^{1/2}\right]$. On the other hand, equation (4) can be rewritten as:

$$\varnothing_{\Delta T}\left(|K|\right)^{1/2} = C\mathrm{e}^{-2|k|Z_0}\left(\mathrm{e}^{-|k|(z_t - z_0)} - \mathrm{e}^{-|k|(z_b - z_0)}\right) \tag{6}$$

where, C is constant. For the long-wavelength segment, Equation (6) can be rewritten as:

$$\varnothing_{\Delta T}\left(|K|\right)^{1/2} = C\mathrm{e}^{-2|k|Z_0}\left(\mathrm{e}^{-|k|(-d)} - \mathrm{e}^{-|k|(d)}\right) \tag{7}$$

Equation (7) can be rewritten as follows:

$$\varnothing_{\Delta T}\left(|K|\right)^{1/2} \approx C\mathrm{e}^{-|k|Z_0} 2|k|d\,, \tag{8}$$

where, $2d$ is the thickness of the magnetic source, from Equation (8), it can be expressed as:

$$\ln\left\{\frac{\varnothing_{\Delta T}\left(|K|\right)^{1/2}}{|K|}\right\} = \ln D - |K| Z_0 \tag{9}$$

where, D is a constant. The centroid of the magnetic source Z_0 can be estimated by fitting a straight line through the low-wavenumber part of the radially averaged frequency-scaled power spectrum

$$\ln\left\{\frac{\varnothing_{\Delta T}\left(|K|\right)^{1/2}}{|K|}\right\}$$

From the slope of the power spectrum, we can estimate the depth Z_t of the magnetic layer top surface and central depth Z_0, and the basal depth Z_b of the magnetic layer bottom surface can be computed from Equation (10) ([28] [36]):

$$Z_b = 2Z_0 - Z_t \tag{10}$$

The depth of the bottom of the magnetic object is considered the same as the CPD. Whereas, the basal depth (Z_b) that is calculated from spectral analysis of the magnetic is the CPD ([28] [34]). At this depth, the temperature reaches 580˚C to establish a relation between the Z_b (CPD) and the Curie point temperature (580˚C), the vertical direction of temperature variation and the constant thermal gradient were assumed. The geothermal gradient ($\mathrm{d}T/\mathrm{d}Z$) between the earth's surface and the CPD (Z_b) can be obtained by using the Curie temperature of 580˚C according to Equation (11) ([36] [37] [39]):

$$\mathrm{d}T/\mathrm{dZ} = 580^\circ\mathrm{C}/Z_b \tag{11}$$

Using Fourier's law [40], the heat flow and thermal gradient values can be calculated with the following formula:

$$Q = \lambda\left(580^{\circ}\mathrm{C}/Z_b\right) \tag{12}$$

where Q is the heat flow and λ is the coefficient of thermal conductivity.

The CPD is inversely proportional to heat flow, as shown in Equation (11). This equation assumes that the direction of the temperature variation is vertical and the temperature gradient is constant.

According to Dimitriadis *et al.* (1987) [41] and Nwobgo (1998) [42], they stated that the window size should be at least 4 - 6 times the depth of the Curie surface. The study area was divided into 32 windows. The size of each window is approximately 60 × 60 km, with an overlapping sliding window to calculate the entire area, and each of the two adjacent windows overlaps by 30 km using the Oasis Montajprogramme (2007) [30]. The RTP map (**Figure 3**) was divided into 32 regions (**Figure 4**) in order to estimate the CPD.

The inclusion of points at the study area boundaries and the extension of the airborne magnetic data used to 30 km around the study area were considered during the calculation to calculate the CPD at these points to cover the study area. The coordinates in the centre of each window, representing the sample point, were used to plot the calculated CPD (**Figure 4**).

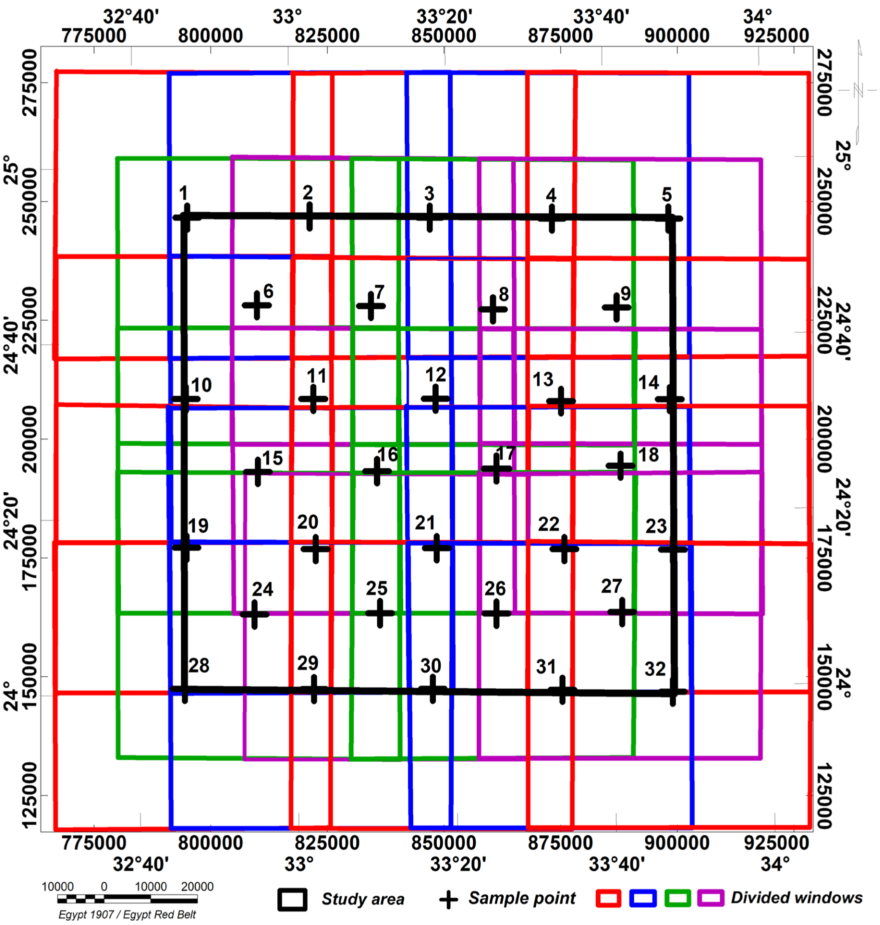

Figure 4. Location map of the study area showing the 32 areas used to estimate the depth to the centroid and top of the magnetic sources.

The 2-D FFT power spectrum method (Equations (5) and (9)) was applied to each window. Using these two equations, the amplitude spectrum of every window and the ratio between the amplitude spectrum and wavenumber were calculated to obtain an estimation value for the buried depth (Z_t) of the magnetic body top surface and the centroid depth of the magnetic body (Z_0). Z_t and Z_0 were derived from the slope of the second-longest wavelengths of the radially averaged power spectrum $\ln\left[\varnothing_{\Delta T}\left(|K|\right)^{1/2}\right]$ and the longest slope of the frequency-scaled power spectrum $\ln\left\{\frac{\varnothing_{\Delta T}\left(|K|\right)^{1/2}}{|K|}\right\}$. **Figure 5** shows the calculated depth to the top of the magnetic bodies (Z_t) for No. 14 from the radially average power spectrum. **Figure 6** shows the estimated centroid depth of magnetic bodies (Z_0) for window No. 14 as an example of the radially averaged power spectrum applied to each window of the 32 windows.

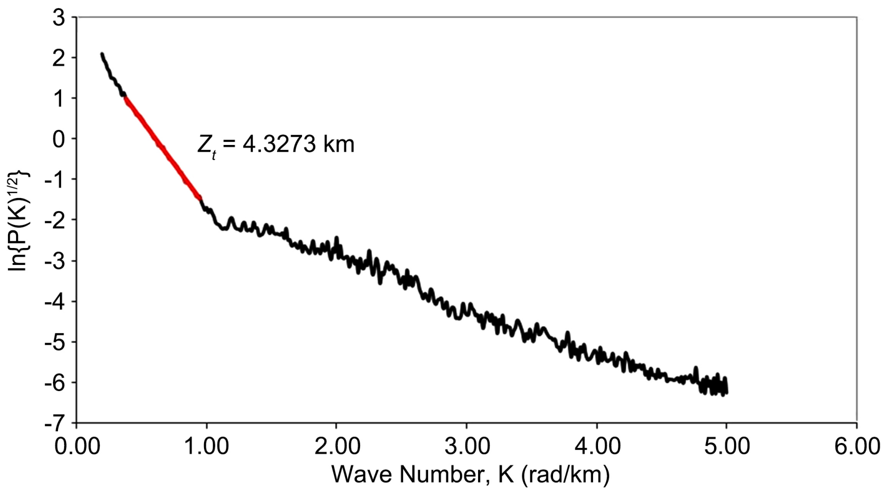

Figure 5. Radially averaged power spectrum used for estimating the depth to the top of the magnetic bodies (Z_t) of window No. 14.

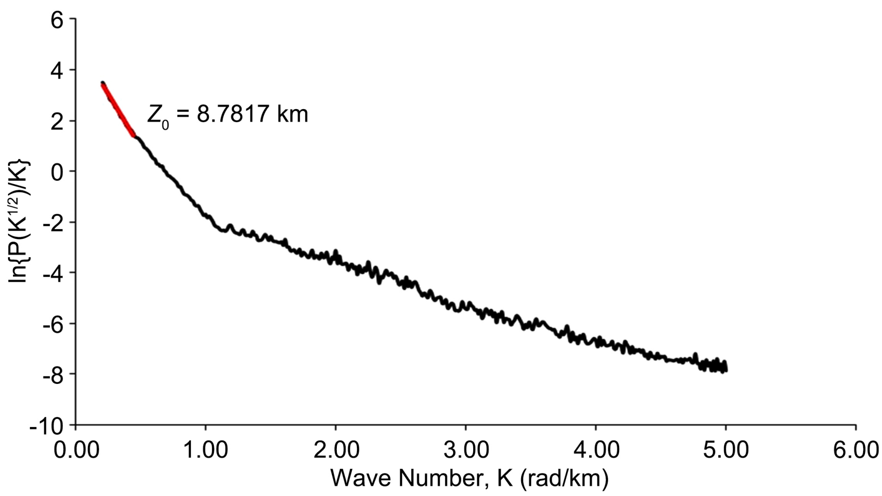

Figure 6. Radially averaged power spectrum used for estimating the centroid depth (Z_0) of window No. 14 areas.

After calculation of (Z_t) and (Z_0), the depth to the bottom of the magnetic source bodies (Z_b) was calculated using Equation (10), which represents the CPD. The geothermal gradient ($\mathrm{d}T/\mathrm{d}Z$) and the surface heat flow (Q) were calculated using Equations (11) and (12), respectively, for each window in the study area. All these statistics were summarized in Table 1.

5. Results and Discussion

The calculated CPD values were gridded to show the variation in depth to the bottom of the magnetic objects (CPD), as shown in Figure 7. The isothermal depth map (Figure 7) of the study area shows that the CPD values range from 13 km to 20 km (Table 1). The isothermal depth map (Figure 7) shows that the depth decreases in four regions within the study area. These regions are assigned as A, B, C, and D on the Curie-isotherm depth map (Figure 7). The depths in these regions reach 13 km. The rest of the study area has an average depth of about 17 Km. On the other hand, the depth increases in some parts to 20 Km.

The corresponding geothermal gradient ranges from 43 to 27˚C/km. The geothermal gradient map (Figure 8) shows that the average value of the geothermal gradient for the majority of the study area is 30˚C/km. Four regions (A, B, C, and D) have a high geothermal gradient of more than 35˚C/km that reaches, in some locations, to 43˚C/km (Figure 8).

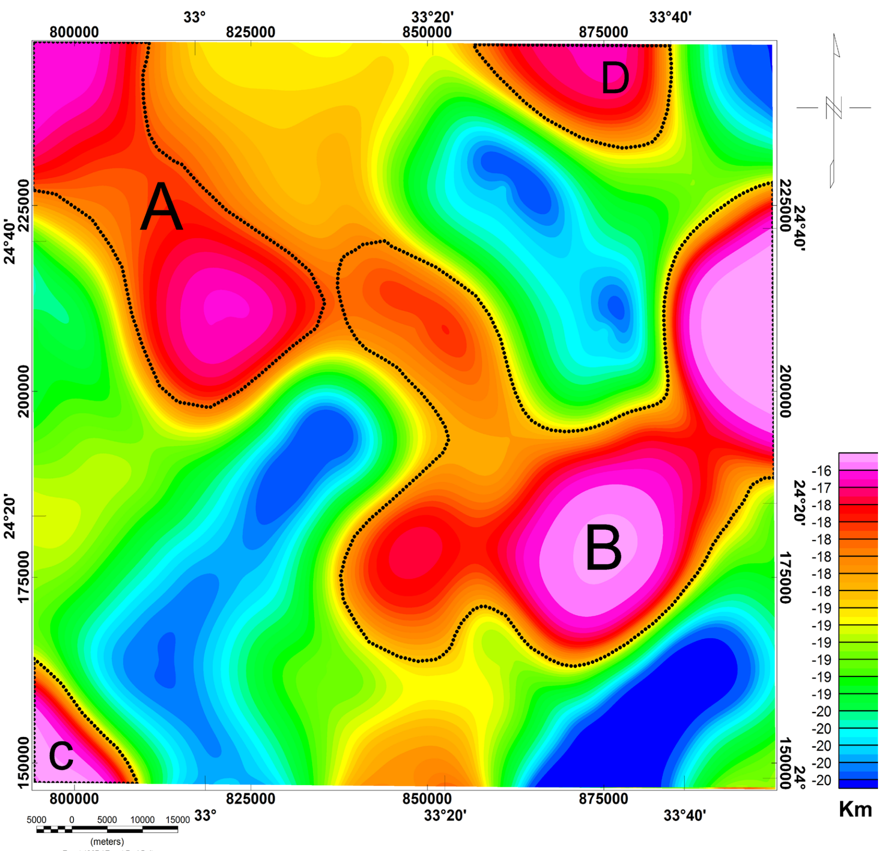

Figure 7. Curie-isotherm depth map of the study area.

Table 1. Results of depth estimations for the top (Z_t) and centroid (Z_0) of magnetic source bodies, as well as the CPD (Z_b) with corresponding geothermal gradient (dT/dZ) and heat flow (Q) for all divided windows.

Area No.	Z_t (Km)	Z_0 (Km)	Z_b (Km)	dT/dZ (°C/Km)	Q (mW/m^2)
1	4.70	10.66	16.62	34.90	87.24
2	5.34	11.98	18.61	31.16	77.90
3	5.72	12.19	18.65	31.10	77.74
4	5.71	11.42	17.12	33.87	84.67
5	4.71	12.54	20.36	28.48	71.20
6	5.15	11.53	17.92	32.37	80.94
7	5.39	11.94	18.49	31.37	78.42
8	4.85	12.42	20.00	29.00	72.50
9	4.34	11.63	18.92	30.65	76.63
10	4.62	11.98	19.34	29.99	74.97
11	6.67	11.85	17.03	34.05	85.13
12	6.67	12.32	17.98	32.25	80.62
13	4.13	12.01	19.88	29.17	72.92
14	4.33	8.78	13.24	43.82	109.55
15	4.68	11.79	18.91	30.67	76.68
16	5.26	12.73	20.19	28.72	71.80
17	4.18	11.26	18.35	31.61	79.03
18	4.30	10.93	17.56	33.03	82.58
19	5.63	12.23	18.83	30.80	76.99
20	4.48	12.27	20.05	28.93	72.32
21	3.56	10.54	17.52	33.11	82.77
22	4.11	9.78	15.45	37.53	93.84
23	4.39	11.78	19.18	30.25	75.62
24	4.54	12.33	20.11	28.84	72.09
25	4.79	11.88	18.98	30.56	76.40
26	4.63	11.71	18.79	30.86	77.15
27	4.31	12.44	20.56	28.21	70.53
28	4.31	10.07	15.82	36.67	91.67
29	0.00 (Basement is exposed to the surface)	10.00	20.00	29.00	72.50
30	5.94	12.11	18.28	31.72	79.30
31	4.21	12.50	20.79	27.90	69.76
32	4.19	11.56	18.93	30.65	76.61

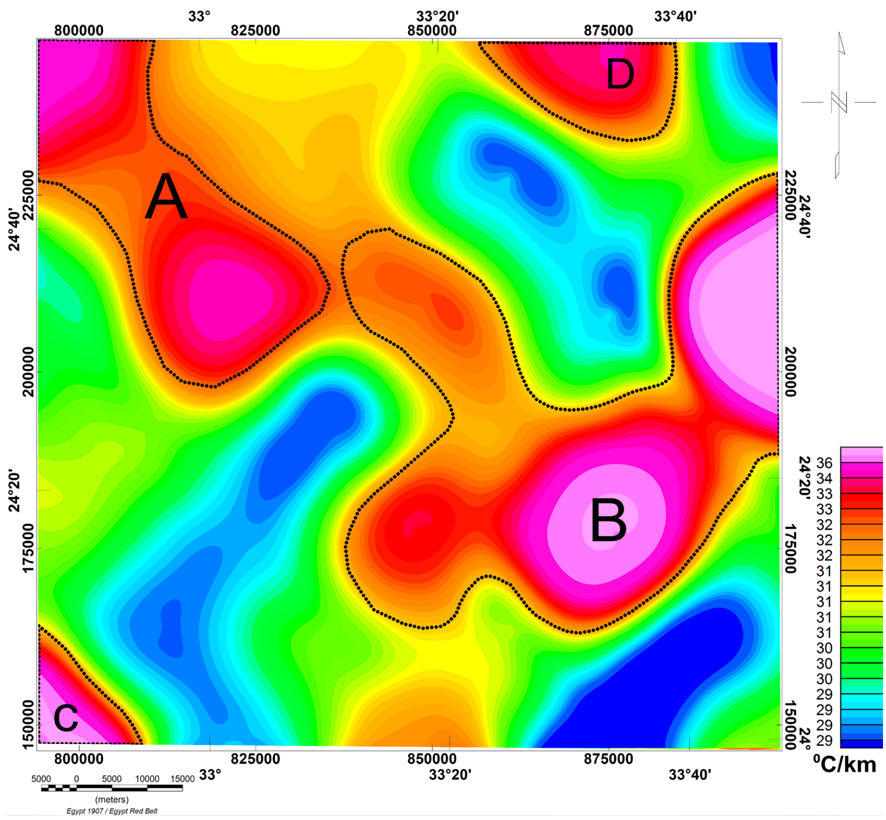

Figure 8. Geothermal gradient map of the study area.

A heat flow map was generated as shown in (Figure 9). The surface heat flow of the study area decreases from 109 to 69 mW/m^2. The CPD varies inversely with both the geothermal gradient and the heat flow. Hence, the heat flow values in the assigned areas A, B, C, and D increase to 109 mW/m^2 (Figure 9). On the other hand, in other parts of the study area, the heat flow ranges from 70 to 85 mW/m^2.

From the spectral analysis of airborne magnetic data in the study area, an average CPD value of about 17 km was calculated, which decreased to 13 Km in some areas (A, B, C, and D) (Figure 7). The average heat flow for the study area is about 80 mW/m^2. Since the Kom-Ombo and Nuqra basins are part of the continental rift of the Red Sea and the Gulf of Suez, the calculated average heat flow in the study area is as the same as the heat flow recorded in the Gulf of Suez, which is 80 mW/m^2 [43]. Due to the absence of magnetite in the upper mantle, the Moho discontinuity is considered to be the lower magnetic boundary [44]. Thus, the calculated bottom depth of the magnetic objects is considered a Moho discontinuity.

The estimated Curie-isotherm depth (Figure 7) is inversely proportional to the geothermal gradient (Figure 8) and heat flow (Figure 9).

The depth of the Moho discontinuity in the northern Western Desert ranges from a depth of more than 35 km to about 30 km at the Mediterranean coast and then decreases rapidly to about 20 km not far from latitude 32˚N [20]. Therefore,

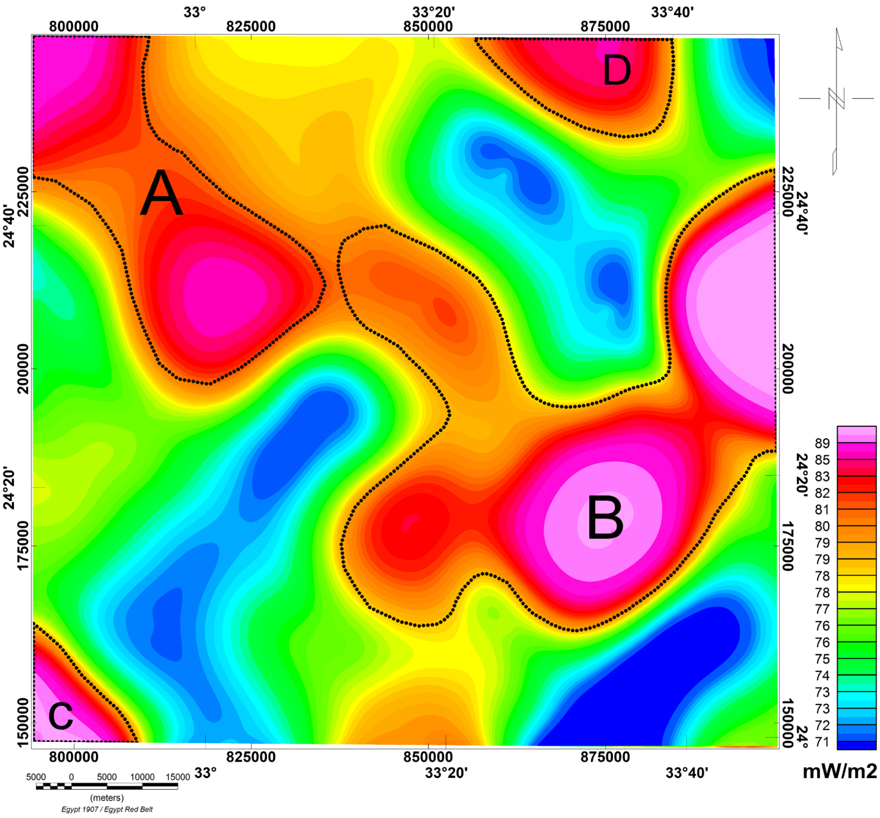

Figure 9. Surface heat flow map of the study area.

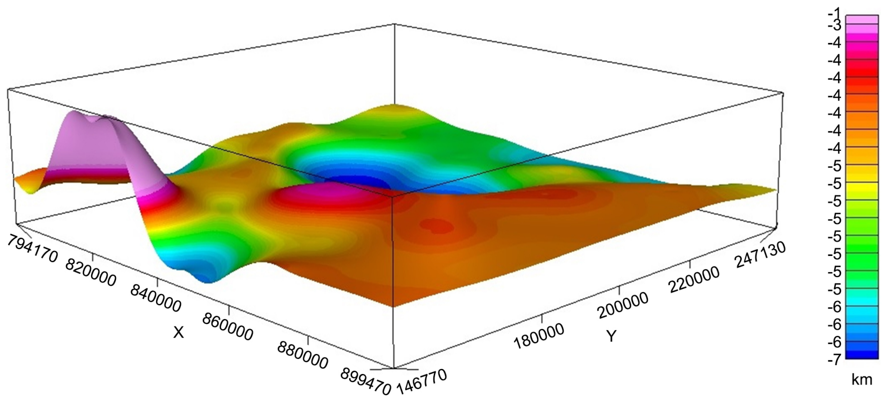

Figure 10. Basement relief based on the calculated depth to the top of the magnetic bodies (Z_t).

we can conclude that the changes of the Moho discontinuity for the study area differ by an average of 17 km. The continental crust is composed largely of radioactive elements compared to the oceanic crust. Sixty percent of the heat on the continents is derived from these radioactive elements [45]. The oil window ranges from 50˚C to 150˚C. Therefore, petroleum is formed at depths ranging from 2.3 to 6.8 km. These depths explain why oil is mainly produced from Cretaceous and older deposits in the study area [20]. The calculated depth to the top of the magnetic bodies (Z_t) ranges from 3.5 - 6.6 km, and this is the main depth range in which petroleum is formed. The 3D model of the depth to the top of the magnetic bodies has been viewed using the Oasis Montaj Programme, 2007 [30] (**Figure 10**).

The heat flow values in the western desert are lower than those in the Gulf of Suez; therefore, the drilling is deeper in the western desert as compared to the Gulf of Suez. As a result, this study recommends deep and moderate drilling for hydrocarbon production in the study area except in areas A, B, C, and D, where the heat flow values reach 109 mW/m^2.

6. Conclusions

In the present study, spectral analysis of magnetic anomaly data was applied to the study area to estimate the Curie-isotherm depth, geothermal gradient, and heat flow over the Kom-Ombo and Nuqra basins in southern Egypt. A surface Curie-isotherm depth calculation was performed based on a spectral analysis of airborne magnetic data. To estimate the depth to the top (Z_t) and bottom (Z_0) of magnetic source objects, the area was divided into 32 windows (regions). The results of this research showed that CPD values range from 13 km to 20 km. The isotherm-depth map (**Figure 7**) shows that the depth decreases in four regions (A, B, C, and D) to 13 km. The average depth of most of the study area is 17 km.

The geothermal gradient corresponding to the study area ranges from 27 to 43˚C/km. The average geothermal gradient value for the majority of the study area is 30˚C/km. The calculated surface heat flow of the study area ranges from 69 to 109 mW/m^2. The heat flow values in the assigned areas A, B, C, and D increase to 109 mW/m^2. On the other hand, in other parts of the study area, the heat flow ranges from 70 to 85 mW/m^2.

The calculated high heat flow values indicate a high probability of hydrocarbon accumulations in the Kom-Ombo and Nuqra basins. Moderate drilling for hydrocarbon production in the study area is recommended except for Areas A, B, C and D, where heat flow values reach 109 mW/m^2.

Conflicts of Interest

The authors declare no conflicts of interest regarding the publication of this paper.

References

[1] Guiraud, R. and Maurin, J.C. (1992) Early Cretaceous Rifts of Western and Central Africa: An Overview. *Tectonophysics*, **213**, 153-168. https://doi.org/10.1016/0040-1951(92)90256-6

[2] Philip, J., Babinot, J. F., Tronchetti, G., Fourcade, E., Ricou, L. E., Guiraud, R., Bellion, Y., Herbin, J. P., Combes, P. J., Cornee, J. J., and Dercourt, J. (1993) Late Cenomanian (94 to 92 Ma). In: Dercourt, J., Ricou, L.E. and Vrielynck, B., Eds., *Atlas Tethys Paleoenvironmental Maps*, Gauthier-Villars, Paris, 153-178.

[3] Abdeen, M.M., Ramadan, F.S., Nabawy, B.S. and El Saadawy, O. (2021) Subsurface Structural Setting and Hydrocarbon Potentiality of the Komombo and Nuqra Ba-

sins, South Egypt: A Seismic and Petrophysical Integrated Study. *Natural Resources Research*, **30**, 3575-3603. https://doi.org/10.1007/s11053-021-09898-2

[4] Taha, M.A. (1992) Mesozoic Rift System in Egypt, Their Southern Extension and Impact on Future Exploration. *Proceedings of the* 11*th Petroleum Exploration and Production Conference*, Cairo, 7-10 November 1992, 1-19.

[5] Taha, M.A. and Abd El-Aziz, H.A. (1998) Mesozoic Rifting in Upper Egypt Concession (abs.). 14*th International Petroleum Conference*.

[6] Yousif, M.S.M. and El-Assy, A.T.E. (1998) Quantitative Study of the Fracture Pattern of the Area around the Western Part of Wadi El-Kharit, South Eastern Desert, Egypt. *The Egyptian Journal of Remote Sensing and Space Sciences*, **1**, 145-163.

[7] Roden, J., Abdelsalam, M.G., Atekwana, E., El Qady, G. and Tarabees, E.A. (2011) Structural Influence on the Evolution of the Pre-Eonile Drainage System of Southern Egypt: Insights from Magnetotelluric and Gravity Data. *Journal of African Earth Sciences*, **61**, 358-368. https://doi.org/10.1016/j.jafrearsci.2011.08.007

[8] Said, M.S. and Sakran, S. (2020) Structural Analysis and Tectonic Evolution of the Komombo Basin, South Egypt; An Example of Interior Cretaceous Rift. *Journal of African Earth Sciences*, **162**, Article ID: 103719. https://doi.org/10.1016/j.jafrearsci.2019.103719

[9] Abu El Ella, N. (2006) Biostratigraphy and Lithostratigraphy of Komombo-1, Komombo-2, Komombo-3, Nuqra-1 and Kharit-1 Wells, Upper Egypt. Earth Resources Exploration (EREX), Unpublished Internal Report, Cairo.

[10] Abu El Ella, N. (2011) Biostratigraphic Studies for the AlBaraka Oil Field, Upper Egypt. Earth Resources Exploration (EREX), Unpublished Internal Report, Cairo.

[11] Ali, M., Darwish, M., Abdelhady, A. and Essa, M.A. (2017) Structural and Lithostratigraphic Evolution of Al Baraka Oil Field, Komombo Basin, Upper Egypt as Deduce from 2D Seismic Lines and Well Logging Data. *Journal of Environmental Sciences*, **4**, 149-169.

[12] Ali, M., Darwish, M., Essa, M.A. and Abdelhady, A. (2018) 2D Seismic Interpretation and Characterization of the Hauterivian-Early Barremian Source Rock in Al Baraka Oil Field, Komombo Basin, Upper Egypt. *Journal of African Earth Sciences*, **139**, 113-119. https://doi.org/10.1016/j.jafrearsci.2017.12.010

[13] Ali, M., Darwish, M., Essa, M.A. and Abdelhady, A. (2019) Comparison of the Dakhla Formation Source Rock Potential between Komombo Basin and Gebel Duwi, Upper Egypt. *Arabian Journal of Geosciences*, **12**, Article No. 613. https://doi.org/10.1007/s12517-019-4833-y

[14] Ali, M., Abdelmaksoud, A., Essa, M.A., Abdelhady, A. and Darwish, M. (2020) 3D Structural, Facies and Petrophysical Modeling of C Member of Six Hills Formation, Komombo Basin, Upper Egypt. *Natural Resources Research*, **29**, 2575-2597. https://doi.org/10.1007/s11053-019-09583-5

[15] Ali, M., Abdelhady, A., Abdelmaksoud, A., Darwish, M. and Essa, M.A. (2020) 3D Static Modeling and Petrographic Aspects of the Albian/Cenomanian Reservoir, Komombo Basin, Upper Egypt. *Natural Resources Research*, **29**, 1259-1281. https://doi.org/10.1007/s11053-019-09521-5

[16] El Nady, M.M., Ramadan, F.S., Hammad, M.M., Mousa, D.A. and Lotfy, N.M. (2018) Hydrocarbon Potentiality and Thermal Maturity of the Cretaceous Rocks in Al Baraka Oil Field, KomOmbo Basin, South Egypt. *Egyptian Journal of Petroleum*, **27**, 1131-1143. https://doi.org/10.1016/j.ejpe.2018.04.003

[17] Selim, S.S. (2016) A New Tectono-Sedimentary Model for Cretaceous Mixed Nonmarine-Marine Oil-Prone Komombo Rift, South Egypt. *International Journal of Earth*

Sciences, **105**, 1387-1415. https://doi.org/10.1007/s00531-015-1260-5

[18] Hosney, H.M. (2000) Geophysical Parameters and Crustal Temperatures Characterizing Tectonic and Heat Flow Provinces of Egypt. Cairo University, Giza, 152-166.

[19] Mohamed, H.S., Abdel Zaher, M., Mahmoud, M. and Senosy, M.M. (2015) Geothermal Gradients in the North Western Desert, Egypt as Deduced from Bottom-Hole Temperature and Aerogravity Data. *Proceedings World Geothermal Congress*, Melbourne, 19-25 April 2015.

[20] Saada, S.A. (2016) Curie Point Depth and Heat Flow from Spectral Analysis of Aeromagnetic Data over the Northern Part of Western Desert, Egypt. *Journal of Applied Geophysics*, **134**, 100-111. https://doi.org/10.1016/j.jappgeo.2016.09.003

[21] Tarshan, A. and Shimanskiy, S. (2019) Petroleum System Modelling and Identification of Promising Oil and Gas Bearing Objects in the Eastern Part of the Gulf of Suez, Egypt. *Russian Journal of Earth Sciences*, **19**, ES4005. https://doi.org/10.2205/2019ES000669

[22] Conoco (1987) Geologic Map of Egypt (20 Sheets, Scale 1:500,000). Egyptian General Authority for Petroleum (UNESCO Joint Map Project), Cairo.

[23] Nabawy, B.S., Rochette, P. and Géraud, Y. (2009) Petrophysical and Magnetic Pore Network Anisotropy of Some Cretaceous Sandstone from Tushka Basin, Egypt. *Geophysical Journal International*, **177**, 43-61. https://doi.org/10.1111/j.1365-246X.2008.04061.x

[24] Nabawy, B.S., Rochette, P. and Géraud, Y. (2010) Electric Pore Fabric of the Nubia Sandstones in South Egypt: Characterization and Modelling. *Geophysical Journal International*, **183**, 681-694. https://doi.org/10.1111/j.1365-246X.2010.04789.x

[25] Aero-Service (1984) Final Report on Airborne Magnetic and Radiation Survey in Eastern Desert, Egypt. Work Completed for the Egyptian General Petroleum Corporation (EGPC). Six Volumes, Aero-Service, Houston.

[26] Blakely, R.J. (1995) Potential Theory in Gravity and Magnetic Applications. Cambridge University Press, Cambridge, 307-308. https://doi.org/10.1017/CBO9780511549816

[27] Li, C.-F., Shi, X., Zhou, Z., Li, J., Geng, J. and Chen, B. (2010) Depths to the Magnetic Layer Bottom in the South China Sea Area and Their Tectonic Implications. *Geophysical Journal International*, **182**, 1229-1247. https://doi.org/10.1111/j.1365-246X.2010.04702.x

[28] Okubo, Y., Graf, R.J., Hansent, R.O., Ogawa, K. and Tsu, H. (1985) Curie Point Depths of the Island of Kyushu and Surrounding Areas Japan. *Geophysics*, **53**, 481-494. https://doi.org/10.1190/1.1441926

[29] Zhou, S. and Thybo, H. (1998) Power Spectra Analysis of Aeromagnetic Data and KTB Susceptibility Logs and Their Implication for Fractal Behavior of Crustal Magnetization. *Pure and Applied Geophysics*, **151**, 147-159. https://doi.org/10.1007/s000240050109

[30] Oasis Montaj (Geosoft Program) (2007) Geosoft Mapping and Application System, Inc, Suit 500, Richmond St. West Toronto, ON Canada N5SIV6.

[31] Thébault, E., Purucker, M., Kathryn, A., Langlais, W.B. and Sabaka, T.J. (2010) The Magnetic Field of the Earth's Lithosphere. *Space Science Reviews*, **155**, 95-127.

[32] Spector, A. and Grant, F.S. (1970) Statistical Models for Interpreting Aeromagnetic Data. *Geophysics*, **35**, 293-302. https://doi.org/10.1190/1.1440092

[33] Shuey, R.T., Schellinger, D.K., Tripp, A.C. and Alley, L.B. (1977) Curie Depth Determination from Aeromagnetic Spectra. *Geophysical Journal International*, **50**,

75-101. https://doi.org/10.1111/j.1365-246X.1977.tb01325.x

[34] Bhattacharyya, B.K and Leu, L.-K. (1975) Analysis of Magnetic Anomalies over Yellowstone National Park: Mapping the Curie Point Isotherm Surface for Geothermal Reconnaissance. *Journal of Geophysical Research*, **80**, 461-465. https://doi.org/10.1029/JB080i032p04461

[35] Bhattacharyya, B.K. anf Leu, L.-K. (1977) Spectral Analysis of Gravity and Magnetic Anomalies due to Rectangular Prismatic Bodies. *Geophysics*, **42**, 41-50. https://doi.org/10.1190/1.1440712

[36] Tanaka, A., Okubo, Y. and Matsubayashi, O. (1999) Curie Point Depth Based on Spectrum Analysis of the Magnetic Anomaly Data in East and Southeast Asia. *Tectonophysics*, **306**, 461-470. https://doi.org/10.1016/S0040-1951(99)00072-4

[37] Maden, N. (2010) Curie-Point Depth from Spectral Analysis of Magnetic Data in Erciyes Stratovolcano (Central TURKEY). *Pure and Applied Geophysics*, **167**, 349-358. https://doi.org/10.1007/s00024-009-0017-0

[38] Saibi, H., Aboud, E. and Gottsmann, J. (2015) Curie Point Depth from Spectral Analysis of Aeromagnetic Data for Geothermal Reconnaissance in Afghanistan. *Journal of African Earth Sciences*, **111**, 92-99. https://doi.org/10.1016/j.jafrearsci.2015.07.019

[39] Stampolidis, A., Kane, I., Tsokas, G.N. and Tsourlos, P. (2005) Curie Point Depths of Albania Inferred from Ground Total Field Magnetic Data. *Surveys in Geophysics*, **26**, 461-480. https://doi.org/10.1007/s10712-005-7886-2

[40] Fourier, J. (1955) Analytical Theory of Heat. Dover Publications, New York.

[41] Dimitriadis, K., Tselentis, G.-A. and Thanassoulas, K. (1987) A BASIC Program for 2-D Spectral Analysis of Gravity Data and Source-Depth Estimation. *Computers & Geosciences*, **13**, 549-560. https://doi.org/10.1016/0098-3004(87)90056-2

[42] Nwobgo, P.O. (1998) Spectral Prediction of Magnetic Source Depths from Simple Numerical Models. *Computers & Geosciences*, **24**, 847-852. https://doi.org/10.1016/S0098-3004(97)00131-3

[43] Feinstein, S., Kohn, B.P., Steckler, M.S. and Eyal, M. (1996) Thermal History of the Eastern Margin of the Gulf of Suez, I. Reconstruction from Borehole Temperature and Organic Maturity Measurements. *Tectonophysics*, **266**, 203-220. https://doi.org/10.1016/S0040-1951(96)00190-4

[44] Wasilewski, P.J., Thomas, H.H. and Mayhew, M.A. (1979) The Moho as a Magnetic Boundary. *Geophysical Research Letters*, **6**, 541-544. https://doi.org/10.1029/GL006i007p00541

[45] Glassley, W.E. (2010) Geothermal Energy: Renewable Energy and the Environment. CRC Press, Boca Raton, 276 p.